

Disordered spherical bead packs are anisotropic

This article has been downloaded from IOPscience. Please scroll down to see the full text article.

2010 EPL 90 34001

(<http://iopscience.iop.org/0295-5075/90/3/34001>)

View [the table of contents for this issue](#), or go to the [journal homepage](#) for more

Download details:

IP Address: 138.194.34.46

The article was downloaded on 10/05/2010 at 02:58

Please note that [terms and conditions apply](#).

Disordered spherical bead packs are anisotropic

G. E. SCHRÖDER-TURK^{1(a)}, W. MICKEL¹, M. SCHRÖTER², G. W. DELANEY³, M. SAADATFAR^{5,4}, T. J. SENDEN⁵, K. MECKE¹ and T. ASTE^{5,6}

¹ *Theoretische Physik, Fried.-Alex.-Universität Erlangen-Nürnberg - Staudtstr. 7, 91058 Erlangen, Germany, EU*

² *Center for Nonlinear Dynamics and Department of Physics, University of Texas - Austin, TX 78712, USA*

³ *CSIRO Mathematics, Informatics and Statistics - Private Bag 33, Clayton South, Victoria 3168, Australia*

⁴ *Foams and Complex Systems, School of Physics, Trinity College Dublin - Dublin, Ireland, EU*

⁵ *Department of Applied Mathematics, Research School of Physics and Engineering, The Australian National University Canberra ACT 0200, Australia*

⁶ *School of Physical Sciences, University of Kent, Canterbury - Kent, CT2 7NH, UK, EU*

received on 14 April 2010; accepted by U. Seifert on 21 April 2010

published online 7 May 2010

PACS 45.70.-n – Granular systems

PACS 45.70.Cc – Static sand piles; granular compaction

PACS 05.65.+b – Self-organized systems

Abstract – Investigating how tightly objects pack space is a long-standing problem, with relevance for many disciplines from discrete mathematics to the theory of glasses. Here we report on the fundamental yet so far overlooked geometric property that disordered mono-disperse spherical bead packs have significant local structural anisotropy manifest in the shape of the free space associated with each bead. Jammed disordered packings from several types of experiments and simulations reveal very similar values of the cell anisotropy, showing a linear decrease with packing fraction. Strong deviations from this trend are observed for unjammed configurations and for partially crystalline packings above 64%. These findings suggest an inherent geometrical reason why, in disordered packings, anisotropic shapes can fill space more efficiently than spheres, and have implications for packing effects in non-spherical liquid crystals, foams and structural glasses.

open access

editor's choice

Copyright © EPLA, 2010

When frictional spheres of equal size are packed disorderly they can form mechanically stable “jammed” configurations which occupy a fraction of the available volume in the range between 0.55 and 0.64. However, for non-spherical particles this limiting packing fraction has a higher value: it has been recently reported that anisotropic bodies such as M&M chocolate candies pack more tightly than spheres in the disordered phase reaching packing fractions of $\phi \approx 0.71$ for spheroids and $\phi \approx 0.735$ for general ellipsoids [1,2]. Understanding why anisotropic shapes fill space more tightly than spheres is an open question whose answer lies in the complex geometrical properties of disordered packings.

Our study comprises experimental data sets of mechanically stable “jammed”¹ glass bead packs prepared by a fluidised bed method, FB [3], and dry acrylic beads

packs prepared by a tapping/compression method, DA [3]. Coordinates of the bead centres are extracted from 3D X-ray computed tomography images via FFT deconvolution and watershed methods [3,4], with precision better than 0.1% of the sphere diameter. Simulated bead packs of realistic frictional beads are obtained by a discrete element method, DEM [5]. Idealised packs of frictionless spheres undergoing Newtonian dynamics with no gravity are generated by the Lubachevsky-Stillinger Algorithm, LS [6]. Additional unjammed data sets are generated from the bead centre coordinates of the jammed DA data sets by random Monte Carlo moves, MC. The appendix contains details of experiments and simulations.

The shape of the free space around each bead is determined by the Voronoi diagram which is a partition of space into N convex cells $\{K_i\}$ with respect to a set of N points $P = \{\mathbf{r}_i\}$, here the bead centres, such that all points inside the Voronoi cell K_i are closer to r_i than to any of the other points $r_j \in P$ with $i \neq j$, see fig. 1. Voronoi diagrams are computed with *qhull* [7] for all beads in the data set, taking periodic boundary conditions into account

^(a)E-mail: Gerd.Schroeder-Turk@physik.uni-erlangen.de

¹Different definitions of what constitutes the “jammed” state have been given. As a minimal common property, all “jammed” packings analysed here are “locally jammed”, *i.e.* each sphere is held in place by its neighbours.

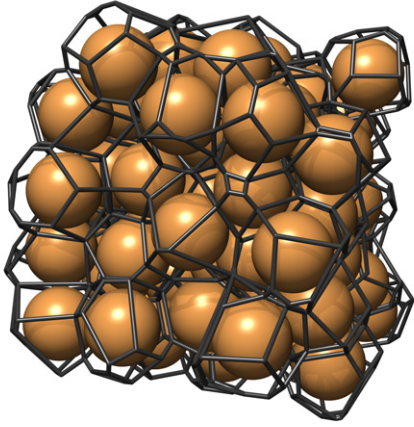


Fig. 1: (Colour on-line) A subset of a jammed disordered packing of beads in 3D with the corresponding Voronoi diagram. The Voronoi cell is the region of space around a bead that is closer to this bead than to any other in the packing. The configuration is a subset of the DA dataset with packing fraction $\phi = 0.586$. See also the supplementary animation clip `BeadsVoronoi.avi`.

for the LS data. Except for the LS data, the statistical analysis is restricted to those beads with a distance of three or more bead diameters to the container walls. The symbol $\langle \rangle$ denotes unweighted averages over these internal beads. The overall packing fraction is $\phi := \frac{4\pi}{3}\sigma^3/\langle W_0 \rangle$, where $\langle W_0 \rangle$ is the average volume of the Voronoi cells in the packing. Neglecting boundary effects, this yields the usual definition $\frac{4\pi}{3}\sigma^3 N/V$, where V is the volume of the container up to the fill height and N is the number of beads.

Minkowski tensors as anisotropy indices. – The Voronoi cells’ anisotropy is quantified by ratios of smallest to largest eigenvalues of *Minkowski tensors*². Minkowski tensors, similar in spirit to the tensor of inertia, are a family of six independent tensorial shape measures, denoted $\mathbf{W}_0^{20}, \mathbf{W}_1^{20}, \mathbf{W}_2^{20}, \mathbf{W}_3^{20}, \mathbf{W}_1^{02}$ and \mathbf{W}_2^{02} , each characterising different aspects of the shape of a body K [8–12]. Each of the six eigenvalue ratios $\beta_\nu^{rs} = |\mu_{\min}/\mu_{\max}| \in [0, 1]$, where μ_{\max} and μ_{\min} are the eigenvalues of the symmetric matrix $\mathbf{W}_\nu^{rs}(K)$ of largest and smallest absolute value, quantifies the degree of anisotropy of the body K with respect to the corresponding Minkowski tensor. An isotropic body has $\beta_\nu^{rs} = 1$ and deviations from 1 quantify the degree of anisotropy of K . These measures are independent of the orientation of K and characterise solely the deviations from sphericity or cubicity [13,14].

For a convex body K in Euclidean 3D space with bounding surface ∂K (here a Voronoi cell) Minkowski tensors are defined as surface integrals of tensor-valued

²Minkowski tensor software is available at www.theorie1.physik.uni-erlangen/karambola.

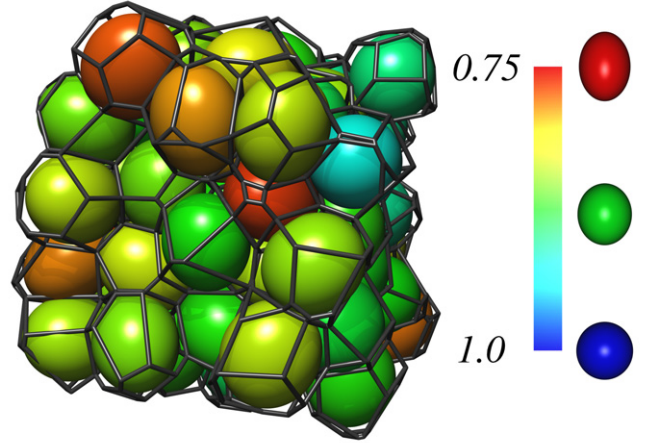


Fig. 2: (Colour on-line) The same subset of the Voronoi diagram as shown in fig. 1, however with the beads replaced by ellipsoids that match the anisotropy and orientation of the Voronoi cells. The anisotropy is quantified by the eigenvalue ratios β_0^{20} of \mathbf{W}_0^{20} of the Voronoi cells. Colours represent the ratio of the shortest and longest axis of the ellipsoid. An isotropic cell has $\beta_0^{20} = 1$ and deviations from 1 quantify anisotropy. An ellipsoid with axes (a, a, c) with shortest-to-longest axis ratio $a/c = 0.8$ corresponds to $\beta_0^{20} \approx 0.65$. See also the supplementary animation clip `EllipsoidsVoronoi.avi`.

products of bounding surface normals \mathbf{n} and position vectors \mathbf{r} and as volume integrals of powers of \mathbf{r} (omitting conventional but irrelevant prefactors):

$$\mathbf{W}_0^{20} = \int_K \mathbf{r}^2 dV, \quad (1)$$

$$\mathbf{W}_1^{20} = \int_S \mathbf{r}^2 dA, \quad \mathbf{W}_1^{02} = \int_S [\mathbf{n}(\mathbf{r})]^2 dA, \quad (2)$$

$$\mathbf{W}_2^{20} = \int_S \mathbf{r}^2 H(\mathbf{r}) dA, \quad \mathbf{W}_2^{02} = \int_S [\mathbf{n}(\mathbf{r})]^2 H(\mathbf{r}) dA, \quad (3)$$

$$\mathbf{W}_3^{20} = \int_S \mathbf{r}^2 G(\mathbf{r}) dA. \quad (4)$$

The vector product is defined as the dyadic product $(\mathbf{a} \otimes \mathbf{b})_{ij} := (a_i b_j + a_j b_i)/2$, *i.e.* $\mathbf{n}^2 = \mathbf{n} \otimes \mathbf{n}$ and $\mathbf{r}^2 = \mathbf{r} \otimes \mathbf{r}$ are rank-2 tensors. $H(\mathbf{r})$ is the mean curvature of S at point \mathbf{r} and $G(\mathbf{r})$ the Gaussian curvature. For a convex polytope, the normal $\mathbf{n}(\mathbf{r})$ along an edge is defined as the average of the two adjacent facet normals, $H(\mathbf{r})$ is one-half the angle between the adjacent facet normals, and $G(\mathbf{r})$ at its vertices is 2π minus the sum of adjacent triangle angles [15]. For all tensors \mathbf{W}_ν^{20} local coordinates are used for each Voronoi cell with the bead centre at the origin.

The six independent rank-2 Minkowski tensors in eqs. (2) to (4) characterise different aspects of the shape of the body K . For example, \mathbf{W}_0^{20} is a measure of the volume mass distribution of a homogeneous body K , \mathbf{W}_1^{20} is a measure of the surface mass distribution of the boundary ∂K of K , and \mathbf{W}_1^{02} is a measure of the area-weighted distribution of facet normals. Minkowski

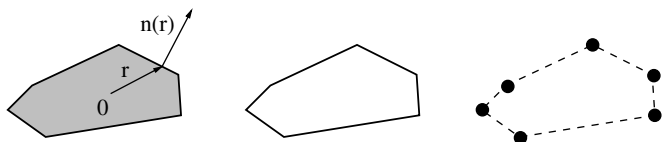


Fig. 3: A 2D solid body, a hollow body, and a body made of disks at the vertices of a convex polygon. Also shown is the position vector \mathbf{r} , with respect to a given origin $\mathbf{0}$, and the surface normal vector \mathbf{n} . For all data in this article the origin $\mathbf{0}$ is chosen as the sphere centre. The corresponding 3D cases are a solid filled body, a hollow body with solid facets, a body made of a wire frame along the polytope edges, and a body made of spheres at the vertices.

tensors are generalisations of surface area and volume to tensor-valued quantities, and hence capable of characterising anisotropy. Essentially, using eigenvalue ratios of the Minkowski tensors to quantify the local anisotropy corresponds to different ways of fitting an ellipsoid to the Voronoi cell K , see fig. 2, for example matching the volume distribution if the cell is considered solid (\mathbf{W}_0^{20}) or hollow (\mathbf{W}_1^{20}), or matching the distribution of facet normals (\mathbf{W}_1^{02}), see also fig. 3. The relevance of Minkowski tensors is underlined by Alesker's theorem stating that any additive motion-covariant continuous functional $f(K)$ is a linear combination of these six Minkowski tensors and scalar Minkowski functionals [9]. The exact computation of all Minkowski tensors is fast and simple, corresponding to sums of edge angles, normal and position vectors and triangle areas [15].

Anisotropy of spherical bead packs. – Figure 4(a) shows the anisotropy indices $\langle \beta_\nu^{rs} \rangle$ as a function of ϕ for jammed bead configurations, both experimental and simulated. The average eigenvalue ratio $\langle \beta_\nu^{rs} \rangle$ demonstrates that there is a significant degree of anisotropy for packings with $\phi < 0.64$ that decreases approximately linearly with increasing ϕ . There is no significant difference between the experimental data from the different preparation methods and the simulated data both with and without gravity. The coincidence between the datasets with friction (DA, FB, DEM) and the simulations without friction (LS) suggests that this result is independent of friction. The fact that this behaviour is similar for all six anisotropy measures β_ν^{rs} demonstrates that the anisotropy is a robust feature of the Voronoi cells, independent of the specific way of determining the corresponding ellipsoid. The data in fig. 4 also shows that anisotropy as a function of packing fraction has a change in slope near $\phi \approx 0.64$. This is the packing fraction at which crystalline nuclei start to form in the LS system. (This transition is even more evident in fig. 5 where the thick + symbols represent the same data for β_1^{02} as above with the linear trend below $\phi \simeq 0.64$ subtracted.)

For all jammed data sets with $\phi < 0.64$ the scaled distribution of the anisotropy indices is similar for all samples and all β_ν^{rs} , and resembles a Gamma distribution (fig. 4(b)). This is similar to what is observed for the distribution of Voronoi volumes [3]. Notably, the probability of

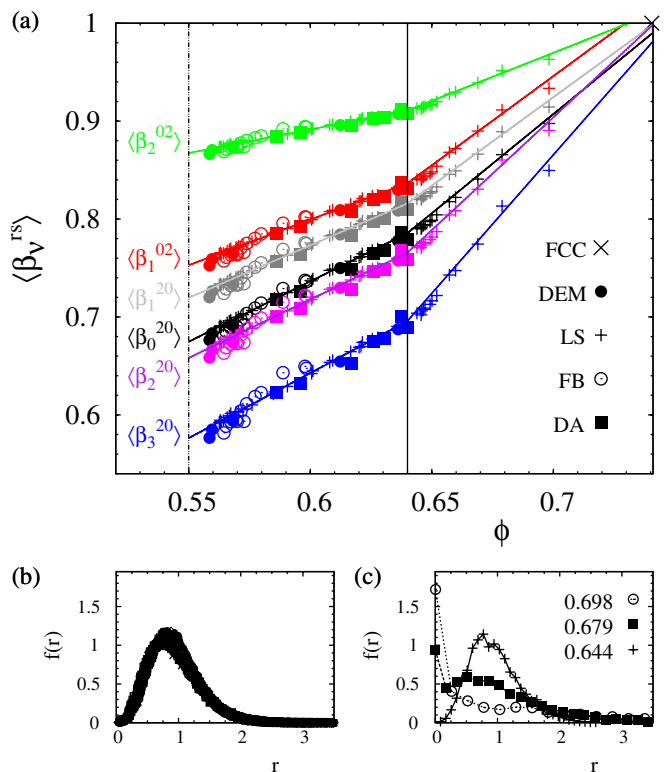


Fig. 4: (Colour on-line) (a) Average anisotropy of the Voronoi cells, measured by averaged eigenvalue ratios $\langle \beta_\nu^{rs} \rangle$ of Minkowski tensors \mathbf{W}_ν^{rs} , as a function of packing fraction ϕ for jammed bead configurations. Isotropic cells have $\beta_\nu^{rs} = 1$ and deviations from 1 measure the degree of anisotropy. The straight lines are linear fits for $\phi < 0.64$ and $\phi > 0.64$. (b) Rescaled distribution of all six anisotropy indices β_ν^{rs} for all experimental and simulated bead packs with $0.55 < \phi < 0.64$, with $r = (1/\beta_\nu^{rs} - 1)/(1/\langle \beta_\nu^{rs} \rangle - 1)$, showing a vanishing probability for isotropic cells ($r = 0$). (c) The same distribution (with identical axes) for β_0^{20} of the Lubachevsky-Stilinger configurations only with packing fractions $\phi = 0.644, 0.679, 0.698$. The finite probability for isotropic cells is an indication of the presence of semi-crystalline regions.

isotropic Voronoi cells, *i.e.* with $\beta_\nu^{rs} = 1$, is close to zero for disordered jammed data sets (fig. 4(b)). Conversely, the distributions for the LS configurations with $\phi > 0.64$, shown in fig. 4(c), depend on ϕ and reveal a finite probability for isotropic Voronoi cells. This is the signature of the presence of crystalline regions above $\phi \approx 0.64$ that increases with the packing fraction.

The analysis in fig. 5 of unjammed data sets generated with LS and MC shows that these configurations are significantly more isotropic than the jammed ones at the same packing fraction. At their respective jamming point these configurations are maximally anisotropic. Further, for a sequence of unjammed configurations that approaches its jamming point and then continues through increasingly dense jammed configurations, $\langle \beta \rangle(\phi)$ shows a distinct change in trend at the jamming point. Note that $\langle \beta \rangle(\phi)$ for unjammed configurations must be process-dependent. A description of the functional form of $\langle \beta_\nu^{rs} \rangle(\phi)$ for

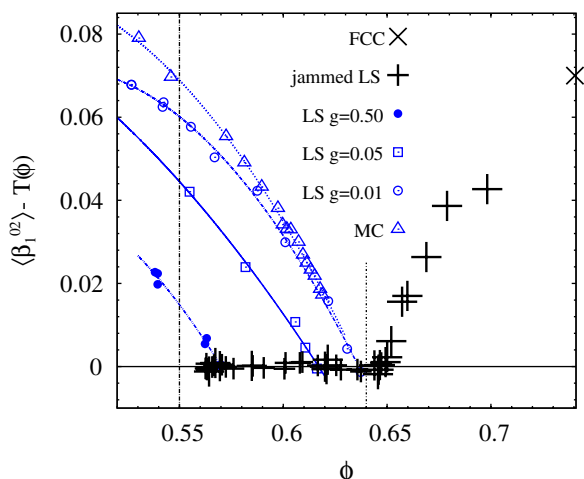


Fig. 5: (Colour on-line) Anisotropy index $\langle \beta_1^{02} \rangle$ for jammed and unjammed configurations generated by the LS algorithm, after subtraction of the linear trend below $\phi = 0.64$. The symbols (+) correspond to jammed LS configurations, the same as in fig. 4, minus the linear fit $T(\phi)$ to all data points of $\langle \beta_1^{02} \rangle$ with $0.55 \leq \phi \leq 0.64$. A distinct change of the slope $d\langle \beta_1^{02} \rangle/d\phi$ is evident at $\phi \approx 0.64$. Squares and circles correspond to *unjammed* configurations for different growth rates g of the LS algorithm. Also shown are unjammed configurations from MC simulations (Δ). Data for all other $\langle \beta_\nu^{rs} \rangle$, not shown for the sake of clarity, are qualitatively similar. Anisotropy is closely tied to jamming while more isotropic configurations exist at the same packing fraction.

the unjammed datasets as ϕ approaches the respective jamming points ϕ_j may contain useful information for the interpretation of $\langle \beta_\nu^{rs} \rangle(\phi)$ as a structural order parameter, but is beyond the scope of this article.

A correlation between the anisotropy of a Voronoi cell and its volume exists and appears to be the same for all jammed configurations and all volume fractions $0.55 < \phi < 0.64$. It becomes evident when introducing a *local packing fraction* $\varphi(K) = V_{sp}/W_0(K)$ for each Voronoi cell, with the sphere volume $V_{sp} = \pi/6$, and considering averages of the anisotropy measures β_ν^{rs} over all cells with a given local volume fraction. Figure 6 shows the average $\langle \beta_0^{20} \rangle_\varphi$ of the anisotropy index β_0^{20} over all Voronoi cells with local packing fraction in the interval $[\varphi, \varphi + \Delta\varphi]$ as a function of φ (with a small $\Delta\varphi \approx 0.01$). The values of $\langle \beta_0^{20} \rangle_\varphi$ for six different data sets (with different global packing fraction ϕ) fall onto a common, approximately linear, curve. Also shown in fig. 6 are the probability distributions $P(\varphi)$ of the local packing fractions of the Voronoi cells (that coincide with the distributions given in [3]). The conclusion of these data is that increased anisotropy in looser jammed datasets is a consequence of an increased number of larger Voronoi cells (that have larger degree of anisotropy). Note that the linear trend of $\langle \beta_0^{20} \rangle_\varphi$ vs. φ in fig. 6 does not extrapolate to 1 for the packing fraction $\varphi_{icos} \approx 0.7546$ that corresponds to the local icosahedral configuration (*i.e.* the locally densest possible configuration).

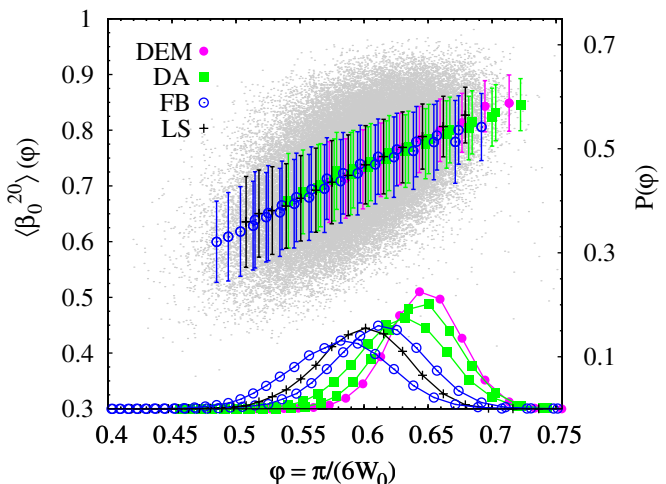


Fig. 6: (Colour on-line) Relationship between local packing fraction $\varphi = (\pi/6)/W_0$ and anisotropy index β_0^{20} . At the bottom (and using the right-hand scale) the distributions $P(\varphi)$ of the local packing fractions are plotted. At the top, the gray scattered points are coordinate pairs $(\varphi(K), \beta_0^{20}(K))$ plotted individually, *i.e.* without any averaging, for each Voronoi cell K in the six samples. The top data points with errorbars represent the averages $\langle \beta_0^{20} \rangle_\varphi$, computed individually for each of the six data sets with a binning of $\Delta\varphi \approx 0.01$. The error bars represent the standard deviations, *i.e.* the width of the distributions of β_0^{20} , and not the negligibly small error of the average. The six datasets shown here have global packing fractions $\phi = 0.567$ (FB), 0.598 (FB), 0.636 (DEM), 0.630 (DA), 0.617 (DA) and 0.585 (LS). Note that the global packing fraction ϕ is given as the average $\langle (\pi/6)/W_0 \rangle$ over all Voronoi cells.

While this analysis demonstrates that the Voronoi cells have a substantial degree of shape anisotropy, an analysis of the average angle between the eigenvectors with maximal or minimal eigenvalue and the vertical axis shows that there is no significant alignment of the cells with the vertical or a horizontal direction, even for the experimental bead packs where gravity is present. The average angle $\langle \xi_0^{20} \rangle$ between the vertical axis and the eigenvector to the maximal eigenvalue of \mathbf{W}_0^{20} (that corresponds for an ellipsoid to the longest axis) is $\pi/4$ for a uniform random distribution of this eigenvector (by convention, eigenvectors point into the upper hemisphere). Consistently, the LS data sets, without gravity, have no statistically significant deviation from the random distribution. Similarly, the DEM, DA and FB data sets yield values of ξ_0^{20} in the interval $[0.23, 0.25]\pi$, indicating only a very slight preference for horizontal orientation of the cells. These deviations from the random orientation are small, in absolute terms and compared to the standard deviation $[\langle (\xi_\nu^{rs})^2 \rangle - \langle \xi_\nu^{rs} \rangle^2]^{1/2} \in [0.142, 0.146]\pi$ for all FB, DA and DEM data sets. Hence, the bead packs are essentially globally isotropic structures composed of anisotropic Voronoi cells with random orientation.

Packings of non-spherical particles. – The observed anisotropy in jammed bead packs suggests that packings of non-spherical bodies should fill space more

tightly than the corresponding packings of spheres. In this respect, the measured degree of anisotropy at $\phi = 0.64$ indicates that the Voronoi cells of jammed spherical beads can, on average, accommodate ellipsoids with axis length ratios $\lambda \approx 0.89$ (corresponding to $\langle \beta_0^{20} \rangle \approx 0.78$). A hypothetical substitution of the beads with such ellipsoids, of larger volume than the spheres, leads to packings with $\phi \approx 0.72$, consistent with experimental and numerical observations for these kinds of packings [2]. It has been argued that the relative increase in packing fraction observed in ellipsoid packings can be related to the increase in the degrees of freedom associated with rotational modes in non-spherical shapes [2,16]. This can be understood in terms of these rotational degrees of freedom allowing the grains to access the inherently anisotropic free space within jammed packings, leading to a better fit and hence to a higher packing fraction overall.

Conclusions. – We have reported on the counterintuitive fact that disordered packings of isotropic objects display strong local anisotropy with vanishing probability to observe isotropic Voronoi cells. Anisotropy is an intrinsic property related to the packing fraction both locally and globally with larger anisotropies for looser packings.

Anisotropy is also associated with the dynamics of structural relaxation and arrest: at a given volume fraction the jammed configuration has the highest degree of anisotropy, at least among the disordered bead packs analyzed here. The generality of this claim needs to be assessed further by analysing, *e.g.*, anisotropic crystalline or inhomogeneous packings taking entropic considerations into account. Additionally, anisotropy is sensitive to local crystallisation showing a clear change in trend with the packing fraction when polycrystalline regions start to form in the simulated samples. This suggests that anisotropy may be an order parameter which can be used to identify subtle structural changes occurring in the packings. These fundamental geometric results, so far overlooked, must be taken into account by theories of jammed packings and has immediate repercussions for experimental approaches to packings of non-spherical particles.

Appendix: Experiments and simulations. –

Dry acrylic beads (DA) and glass beads in fluidised beds (FB). The experimental data sets of bead configurations are from the database on disordered packings [17]. Our study concerns 6 samples (A-F) composed of acrylic beads prepared in air within a cylindrical container with an inner diameter of 55 mm and filled to a height of ~ 75 mm [18–20]. Samples A and C contain ~ 150000 beads with diameter $d = 1.00$ mm and polydispersity within 0.05 mm. Samples B, D-F contain ~ 35000 beads with diameter $d = 1.59$ mm and polydispersity within 0.05 mm. The two samples at lower packing fraction (A, B) were obtained by placing a stick in the middle of the container before pouring the beads and then slowly removing the stick [21]. Sample C was prepared by gently

and slowly pouring the spheres into the container. Sample D was obtained by a faster pouring. In sample E, a higher packing fraction was achieved by gently tapping the container walls. The densest sample (F) was obtained by a combined action of gentle tapping and compression from above (with the upper surface left unconfined at the end of the preparation). To reduce boundary effects, the inside of the cylinder was roughened by randomly gluing spheres to the internal surface. The packing fraction of each of the samples is: A, $\phi \sim 0.586$; B, $\phi \sim 0.596$; C, $\phi \sim 0.617$; D, $\phi \sim 0.626$; E, $\phi \sim 0.630$; and F, $\phi \sim 0.640$.

Twelve other samples (FB14-24 and FB27) containing about 150000 glass beads with diameters 0.25 mm have been also analysed. The packings were prepared in water by means of a fluidised bed technique [3,22] within a vertical polycarbonate tube with an inner diameter of 12.8 mm and a length of 230 mm. Packing fractions between 0.56 and 0.60 were obtained by using different flow rates. After each flow pulse, the particles sediment forming a mechanically stable packing. The grain polydispersity is estimated around 3%.

“Virtual” DEM-relaxed samples without polydispersity.

Numerical samples with almost identical geometrical properties to the experimental samples but without any degree of polydispersity were obtained by using the sphere centre coordinates of experimental data sets and gently relaxing the system to perfect spherical beads.

Our simulation integrates the Newton equation of motion with both translational and rotational degrees of freedoms and under gravity for elasto-frictional spheres. The spheres interact only when overlapping, with a normal repulsive force $F_n = k_n \xi_n^{3/2}$ where $\xi_n = d - |\mathbf{r}_i - \mathbf{r}_j|$ is the overlap between grains of diameters d with centres at \mathbf{r}_i and \mathbf{r}_j [23,24]. Tangential force under oblique loading is also considered as $F_t = -\min(|k_t \xi_n^{1/2} \xi_t|, |\mu F_n|) \cdot \text{sign}(v_t)$, with v_t is relative tangential velocity, and $\xi_t = \int_{t_0}^t v_t(t') dt'$ the displacement in the tangential direction that has taken place since the time t_0 when the two spheres first got in contact integrated over the lifetime of the contact subject to the constraint that during sliding ξ_t is truncated such that the Coulomb friction criteria $F_t \leq \mu F_n$ is satisfied and μ is the kinematic friction coefficient between the spheres [25]. Normal visco-elastic dissipation $F_n = -\gamma_n \xi_n^{1/2} \dot{\xi}_n$ (with $\dot{\xi}_n$ the normal velocity) and a viscous friction force $F_t = -\gamma_t v_t$ [26] are also included.

The DEM relaxation is performed with the initial sphere configuration corresponding to that of the tomographic data. A sub-set of spheres in the central region of the sample is considered, with the boundaries provided by the outer spheres which are kept fixed. The simulation uses realistic physical parameters for acrylic beads: Young modulus 3.2 GPa; Poisson ratio 0.3; density of 1150 kg/m³; inter grain static friction coefficient 0.28. Samples A,C have radius 0.5 mm, samples B,D,E,F have radius 0.795 mm. The glass beads have: Young modulus 70 GPa, a Poisson ratio 0.2; density of 2500 kg/m³; inter

grain static friction coefficient 0.9 and radius 0.125 mm. The final average height of the grains is within 0.1%–0.2% of the initial height and the overall average displacement of the centres of the spheres during the relaxation process is less than 5% of the sphere diameters.

The DEM-relaxation removes polydispersity without substantially modifying the packing configuration. These data sets, included in fig. 4, have negligible difference in anisotropy to the original data sets, demonstrating the robustness of our analysis to small degrees of polydispersity.

Monte Carlo simulations (MC). Simulated unjammed packings (MC), shown as triangles in fig. 5, were obtained by a Monte Carlo simulation method using the positions of the experimental samples as initial conditions and making the system unjammed by reducing the sphere diameters. All these data sets were generated from the experimental data set A by reducing the sphere radius by different amounts generating configurations with different packing fractions, and applying approximately 10^6 canonical Monte Carlo moves (of random direction and random step size between 0 and 20% of the sphere diameter).

Lubachevsky-Stillinger simulations (LS). A set of simulated packings are produced by using a modified Lubachevsky-Stillinger (LS) algorithm [27]. The simulation is an event-driven Newtonian dynamics in which the spheres are considered perfectly elastic without any rotational degree of freedom and with no friction. The simulation is performed in a cubic box with periodic boundary conditions, without gravity. During the simulation, the radii of the spheres are gradually increased from a very loose initial state to more densely packed configurations. In these simulations the principal control parameter is the growth rate for the sphere radii. Small values of growth rates will result in crystallisation. To avoid crystallisation the growth rate should be rather large, forcing the packing into “jammed” non-crystalline structures where the spheres cannot be further expanded at finite pressure [28,29]. Simulations were performed with the code at <http://cherry-pit.princeton.edu/Packing/C++/> with different growth rates g between 2×10^{-5} to 0.5, with initial temperature 0.1, with initial packing fraction 0.1 and with a number of event per cycle equal to 20. In our simulations, packings with $N = 10000$ spheres were generated and the sphere diameters were expanded at a given growth rate until a maximal reduced pressure of 10^{12} was reached [30]. Unjammed configurations are generated using the LS algorithm by stopping expansion at a given packing fraction before the maximal pressure is reached.

REFERENCES

- [1] DONEV A., CISSE I., SACHS D., VARIANO E., STILLINGER F., CONNELLY R., TORQUATO S. and CHAIKIN P., *Science*, **303** (2004) 990.
- [2] MAN W., DONEV A., STILLINGER F., SULLIVAN M., RUSSEL W., HEEGER D., INATI S., TORQUATO S. and CHAIKIN P., *Phys. Rev. Lett.*, **94** (2005) 198001.
- [3] ASTE T., MATTEO T. D., SAADATFAR M., SENDEN T. J., SCHRÖTER M. and SWINNEY H. L., *EPL*, **79** (2007) 24003.
- [4] SAADATFAR M., SHEPPARD A. and KNACKSTEDT M., *Advances in X-ray tomography for Geomaterials* (Wiley) 2006, pp. 269–276.
- [5] DELANEY G., INAGAKI S. and ASTE T., *Fine tuning dem simulations to perform virtual experiments with three-dimensional granular packings*, in *Lect. Notes Complex Syst.*, Vol. **8** (World Scientific) 2007, pp. 169–186.
- [6] LUBACHEVSKY B., STILLINGER F. and PINSON E., *J. Stat. Phys.*, **64** (1991) 501.
- [7] BARBER C., DOBKIN D. and HUHDANPAA H., *ACM Trans. Math. Softw.*, **22** (1996) 469.
- [8] MCMULLEN P., *Rend. Circ. Mat. Palermo, Ser. II*, No. 50 (1997) 259.
- [9] ALESKER S., *Geom. Dedic.*, **74** (1999) 241.
- [10] HUG D., SCHNEIDER R. and SCHUSTER R., *St. Petersburg Math. J.*, **19** (2008) 137.
- [11] HANSEN-GOOS H., ROTH R., MECKE K. and DIETRICH S., *Phys. Rev. Lett.*, **99** (2007) 128101.
- [12] SPORER S., GOLL C. and MECKE K., *Phys. Rev. E*, **78** (2008) 011917.
- [13] BEISBART C., BARBOSA M., WAGNER H. and COSTA L., *Eur. Phys. J. B*, **52** (2006) 531.
- [14] SCHRÖDER-TURK G., KAPFER S., BREIDENBACH B., BEISBART C. and MECKE K., *J. Microsc.*, **238** (2010) 57.
- [15] SCHRÖDER-TURK G., MICKEL W., KAPFER S., HUG D., BREIDENBACH B. and MECKE K., in preparation (2010).
- [16] DELANEY G., WEAIRE D., HUTZLER S. and MURPHY S., *Phil. Mag. Lett.*, **85** (2005) 89.
- [17] See <http://wwrphysse.anu.edu.au/granularmatter/> (2006).
- [18] ASTE T., SAADATFAR M. and SENDEN T. J., *Phys. Rev. E*, **71** (2005) 061302.
- [19] ASTE T., SAADATFAR M., SAKELLARIOU A. and SENDEN T., *Physica A*, **339** (2004) 16.
- [20] ASTE T., *J. Phys.: Condens. Matter*, **17** (2005) S2361.
- [21] ASTE T. and WEAIRE D., *The Pursuit of Perfect Packing* (Institute of Physics Publishing) 2000.
- [22] SCHRÖTER M., GOLDMAN D. and SWINNEY H., *Phys. Rev. E*, **71** (2005) 030301(R).
- [23] LANDAU L. and LIFSHITZ E., *Theory of Elasticity* (Pergamon, New York) 1970.
- [24] MAKSE H. A., GLAND N., JOHNSON D. L. and SCHWARTZ L., *Phys. Rev. E*, **70** (2004) 061302.
- [25] CUNDALL P. A. and STRACK O. D. L., *Geotechnique*, **29** (1979) 47.
- [26] SHÄFER J., DIPPEL S. and WOLF D. E., *J. Phys. I*, **6** (1996) 5.
- [27] SKOGE M., DONEV A., STILLINGER F. H. and TORQUATO S., *Phys. Rev. E*, **74** (2006) 041127.
- [28] TORQUATO S., TRUSKETT T. and DEBENEDETTI P., *Phys. Rev. Lett.*, **84** (2000) 2064.
- [29] RINTOUL M. and TORQUATO S., *Phys. Rev. E*, **58** (1998) 532.
- [30] DONEV A., TORQUATO S., STILLINGER F. H. and CONNELLY R., *Phys. Rev. E*, **71** (2005) 011105.